

# Spontaneous formation of nanostructures during pulsed laser deposition of epitaxial half-Heusler TiNiSn on MgO(001)

R. W. H. Webster, J. E. Halpin, S. R. Popuri, J.-W. G. Bos, and D. A. MacLaren

Citation: [APL Materials](#) **7**, 013206 (2019); doi: 10.1063/1.5052361

View online: <https://doi.org/10.1063/1.5052361>

View Table of Contents: <http://aip.scitation.org/toc/apm/7/1>

Published by the [American Institute of Physics](#)

---

---



The advertisement features a dark blue background. On the left, there is a photograph of the Lake Shore 8600 Series VSM system, which includes a large, dark grey base unit with a control panel and a smaller, black, vertical probe head mounted on a stand. To the right of the image, the Lake Shore CRYOTRONICS logo is displayed in white and blue. Below the logo, the text '8600 Series VSM' is written in a large, bold, orange font. Underneath this, the phrase 'For fast, highly sensitive measurement performance' is written in a smaller, white font. At the bottom right of this text block, there is a small orange button with the text 'LEARN MORE' and a play icon. On the far right, there is a gold-colored award badge with a black border. The badge contains the text '2017' at the top, 'R&D' in large letters, '100' in large letters, and 'WINNER' at the bottom.

**Lake Shore**  
CRYOTRONICS

**8600 Series VSM**

For fast, highly sensitive  
measurement performance

LEARN MORE ►

2017  
**R&D  
100**  
WINNER

# Spontaneous formation of nanostructures during pulsed laser deposition of epitaxial half-Heusler TiNiSn on MgO(001)

Cite as: APL Mater. 7, 013206 (2019); doi: 10.1063/1.5052361

Submitted: 16 August 2018 • Accepted: 30 October 2018 •

Published Online: 17 December 2018



R. W. H. Webster,<sup>1,a)</sup> J. E. Halpin,<sup>1</sup> S. R. Popuri,<sup>2</sup> J.-W. G. Bos,<sup>2</sup> and D. A. MacLaren<sup>1,b)</sup>

## AFFILIATIONS

<sup>1</sup>SUPA, School of Physics and Astronomy, University of Glasgow, Glasgow G12 8QQ, United Kingdom

<sup>2</sup>Institute of Chemical Sciences and Centre for Advanced Energy Storage and Recovery, School of Engineering and Physical Sciences, Heriot-Watt University, Edinburgh EH14 4AS, United Kingdom

<sup>a)</sup>rwebster@physics.org

<sup>b)</sup>dmaclaren@physics.org

## ABSTRACT

The half-Heusler alloy TiNiSn is a promising material for thermoelectric applications that is inexpensive and non-toxic. We demonstrate the epitaxial growth of smooth TiNiSn thin films on MgO(001) single crystal substrates by pulsed laser deposition, using transmission electron microscopy to investigate nanoscale structural and chemical inhomogeneities. In particular, an interfacial reaction results in the formation of a titanium-rich oxide nanolayer at the substrate interface, and this maintains epitaxy but perturbs film composition. Segregation effects are observed throughout the film, producing a narrow range of off-stoichiometric, half-Heusler compositions. The propensity of titanium to oxidise also leads to the commensurate formation of parasitic titanium oxide nanostructures which may be overlooked in bulk techniques but are a key feature that drives both the formation of Ni-enriched, full-Heusler phases and the local decomposition of the half-Heusler to form additional nickel-stannide phases.

© 2018 Author(s). All article content, except where otherwise noted, is licensed under a Creative Commons Attribution (CC BY) license (<http://creativecommons.org/licenses/by/4.0/>). <https://doi.org/10.1063/1.5052361>

Heusler alloys form a remarkably versatile materials system that supports functionalities suitable for a multitude of applications, including spintronics and magneto-optics.<sup>1–3</sup> They have been the focus of substantial materials exploration research,<sup>4–6</sup> and their optimised synthesis, as bulk materials or thin films, is of active concern. This versatility, and capacity for tunability, is of particular interest for the fabrication of thermoelectric generators, which are proposed as a means of scavenging waste heat that could tap into the 60% of energy generated that currently goes unused.<sup>7</sup> In this regard, the semiconducting half-Heusler TiNiSn has emerged as a candidate n-type thermoelectric<sup>8–11</sup> with a reasonable power factor and which—crucially—exploits abundant, non-toxic resources. Improvements in performance have been achieved by doping to independently modulate the electronic character and

introduce structural complexity that can impede thermal transport.<sup>12–17</sup> Such doping, however, also raises questions of phase segregation and stability, particularly when the material synthesis processes may be kinetically limited and conducted far from thermodynamic equilibrium. For example, intrinsic doping with excess Ni has in some studies driven nanoscale segregation into lattice-matched TiNiSn and TiNi<sub>2</sub>Sn phases that scatter phonons.<sup>18–22</sup> Our own recent studies of bulk extrinsic doping with Cu, on the other hand, revealed complex structural characteristics across several length-scales, from micron-scale grain-by-grain variations to nanoscale inclusions.<sup>23</sup> There is, to date, no obvious link between the choice of the bulk synthesis method and the resulting nanostructures that form in doped or off-stoichiometric Heusler alloys. We therefore propose that thin film growth presents a useful

opportunity to fabricate model systems and thereby to explore phase segregation and nanostructuring within the Heusler matrix. To this end, we report the growth of epitaxial TiNiSn by pulsed laser deposition (PLD). The growth of epitaxial TiNiSn on MgO(001) has been demonstrated by other deposition processes,<sup>24–26</sup> but we chose PLD for its ability to produce multi-component films of well-defined stoichiometry and for the increased flexibility in producing non-equilibrium phases and structures.<sup>27</sup> To our knowledge, reports of PLD deposition of thermoelectric Heusler alloys were previously restricted to nanoparticle fabrication.<sup>28</sup> Here, we demonstrate the ability to grow epitaxial thin films of TiNiSn using PLD on single-crystal MgO(001) and use a combination of *in situ* electron diffraction and *ex situ* microscopy to study the resulting nanostructures. We describe an intriguing interfacial reaction in the initial monolayers of deposition, which results in the formation of TiO rather than the more stable TiO<sub>2</sub>, and the distribution of Ni to form a continuum of TiNi<sub>1+x</sub>Sn compositions weighted around three different Heusler phases. Some phase segregation may be driven by the spontaneous production of parasitic titanium monoxide and complementary nickel-stannide phases, which can retain lattice coherence and therefore maintain epitaxy. The nanostructuring of these films illustrates how complexity arises spontaneously within the TiNiSn system, which could be exploited to improve phonon scattering and is likely to be of relevance to an understanding of other Heusler systems.

TiNiSn thin films were deposited by PLD on MgO(001) single crystal substrates (Pi-Kem Ltd., UK) that were first annealed *in situ* under vacuum conditions at 970 K for at least 1 h.<sup>29</sup> The peak-to-peak roughness of these substrates was measured by atomic force microscopy (AFM) to be approximately 4 Å across a 5 μm field of view. MgO has previously been used as a substrate for TiNiSn<sup>24–26</sup> because there is a good lattice match between its periodicity in (110) directions and the TiNiSn unit cell (100) parameter: for an MgO lattice constant of 4.212 Å, the distances are 5.957 Å and 5.936 Å, respectively, giving a lattice mismatch of 0.35%.<sup>9,25</sup> PLD was carried out in a Neocera PLD system using a KrF excimer laser (248 nm, 20 ns pulse duration, typically 200 mJ/pulse at 20 Hz) to ablate a sintered, Ni-rich TiNiSn target material with approximately 1:1:1 composition that was prepared from elemental powders using a protocol described elsewhere<sup>9,17</sup> (Ni enrichment was adopted as it is found to improve thermoelectric performance<sup>9,17</sup>). Energy dispersive x-ray spectroscopy (not shown here) was used to confirm the target uniformity and revealed a few percent of titanium oxides that are common to the use of powder precursors but are not found to impair the material's thermoelectric performance.

Electron energy loss spectroscopy (see below) was used to determine an average film composition of TiNi<sub>1.17</sub>Sn<sub>0.92</sub>, which for ease is referred to as TiNiSn or “half-Heusler” below, together with a 2.5% volume fraction of titanium oxide; differences between the film composition and the nominal target composition may be due to uncertainties in comparing quantitative techniques or may indicate imperfect transfer of stoichiometry during PLD.<sup>30</sup>

Films were deposited at substrate temperatures from room temperature up to 970 K with pressures ranging from a chamber base pressure of 10<sup>−8</sup> Torr up to an argon partial pressure of 10<sup>−2</sup> Torr. The deposition rate was typically 0.01–0.02 nm/s. *In situ* reflection high-energy electron diffraction (RHEED) patterns were recorded throughout deposition using a 30 kV electron source. Films were then characterised *ex situ* by AFM using a Digital Instruments Dimension 3100 atomic force microscope in tapping mode. A protective Pt layer (approx. 30–50 nm thick) was deposited on samples after AFM measurements to avoid subsequent surface oxidation effects. X-ray diffraction (XRD) measurements ( $\theta - 2\theta$ ) were acquired using a PANalytical X'Pert3 diffractometer with a monochromated source of Cu K $\alpha$  radiation.

Thin film samples were first prepared for transmission electron microscopy (TEM) using an FEI Nova Dualbeam focused ion beam (FIB) instrument to prepare cross-sectional lamella by routine methods.<sup>31</sup> TEM and scanning transmission electron microscopy (STEM) data were then acquired using a JEOL ARM200cF probe-corrected instrument that was operated at 200 kV and is equipped with a cold field emission source. Spatially resolved chemical mapping was performed by electron energy loss spectroscopy (EELS) using a Gatan 965 Quantum ER spectrometer to acquire STEM Dual-EELS spectrum images.<sup>32,33</sup> Elemental quantification of EELS spectrum images was aided by a method of absolute quantification that employs a multi-linear least-squares fit to experimentally obtained reference spectra, as described elsewhere.<sup>34–36</sup> The reference-based analysis was essential for accurate quantification since more standard routines were compromised by the proximity of EELS edges, which complicated background subtraction routines, and the known difficulties in using the Hartree-Slater scattering cross sections, whose uncertainty can be as large as 20% for quantification of M edges.<sup>37</sup> Including the considerations detailed by Bobynko *et al.*,<sup>34</sup> contributions from atmospheric oxidation of the lamella surfaces were isolated and amount to <5 nm of encapsulating oxide on the surfaces of the film. Using these methods, compositions are determined with a confidence of 2% accuracy. Some spectra were further analyzed using non-negative matrix factorisation (NMF), which was implemented within the Hyperspy 1.3 package<sup>38</sup> and used to identify and separate common components in the spectra.

The deposition rate for TiNiSn thin films was not observed to vary significantly across the Ar pressure range of 10<sup>−5</sup> mTorr to 10 mTorr, but the RMS roughness (measured across a 5 × 5 μm area by AFM) approximately doubled, with films deposited at base pressure (10<sup>−5</sup> mTorr) appearing smoothest. This may be because low gas pressures enable more energetic species to arrive at the substrate, facilitating intermixing and diffusion. As the aim of this study was to promote epitaxial, smooth films, base pressure was used for subsequent depositions. Deposition temperatures between 300 K and 970 K were assessed, and AFM scans indicated a surface morphological change for films grown above 650 K, with films dewetting from the substrate (and presumably losing Sn) above 800 K. Morphological changes can be seen in panels (a), (b), and (c)

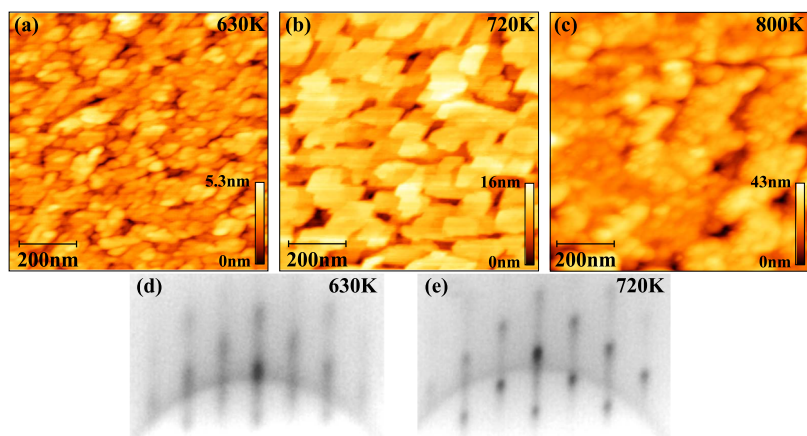


**FIG. 1.** AFM images of the surfaces of ~50–100 nm-thick TiNiSn films grown at substrate temperatures of (a) 630 K, (b) 720 K, and (c) 800 K with [(d) and (e)] the corresponding RHEED patterns for (a) and (b) observed at the end of film growth, collected with the electron beam at a grazing angle to the (100) direction of the MgO substrate. Due to the roughness of the film in (c), no corresponding RHEED pattern was observed.

of Fig. 1, which show AFM surface micrographs of samples grown at 630 K, 720 K, and 800 K, respectively. The images in (a) and (b) highlight a transition from rounded, roughly hemispherical-topped islands with a typical diameter of 30 nm to large, flat islands that span 100–200 nm. Note that the peak-to-peak range in both images is of order 10 nm, substantially less than the film thickness, so that it is clear that the islands have coalesced to completely cover the substrate. At higher temperatures, this is no longer the case, and in Fig. 1(c), dark regions can be seen in the image where the film fails to coalesce, resulting in a peak-to-peak range of 50 nm, which is comparable with the film thickness. Such three-dimensional island formation often arises from limited adatom mobility across step edges during the initial stages of growth.<sup>39</sup> The RHEED patterns in Figs. 1(d) and 1(e) are consistent with the AFM images shown in (a) and (b). In both patterns, the diffraction streaks have a spotty profile that is produced by a three-dimensionally rough surface where the RHEED electron beam is transmitted through the uppermost islands. Neither pattern is sharp, and the diffractive features are broadened in both images, but the diffuse background is strongest for lower deposition temperatures, because of the rougher, less ordered surface. In particular, films grown below 670 K produce a more diffuse specular reflection, indicative of poorer quality crystal growth. Both patterns, however, retain clear diffractive scattering that demonstrates an epitaxial relationship between the substrate and the growing film. In terms of film flatness, we find the optimal deposition temperature to be ~720 K, in agreement with a previous molecular beam epitaxy study<sup>25</sup> which is interesting, given the potential differences in adatom kinetic energies between these two techniques. In that study, although evidence was presented for interfacial roughening, it was not discussed in detail but does suggest that the roughening observed in the present work is not driven by highly energetic sputtering processes, which can occur when PLD is performed under low pressure conditions.<sup>27</sup>

To better understand the thin-film crystal structure, Fig. 2 shows further *in situ* RHEED patterns recorded during deposition of TiNiSn at 720 K. Significant surface roughening and island growth occur during the first 2 monolayers (ML) of

growth, as indicated by the appearance of distinct spots and an increase in diffuse scattering in the pattern [Fig. 2(b)]. (Note that 1 ML is defined here as a single atomic layer of lattice-matched TiNiSn.) At a coverage of 2 ML, new spots appear at one third of the MgO(01) lattice rod spacing, indicating a surface reconstruction, or formation of surface structures, with a periodicity three times that of the bare substrate. This pattern was observed to some degree for all epitaxial films grown above 630 K. Its spotty, transmission-like nature, formed after a single monolayer of deposition, suggests substantial surface re-organisation and roughening that is more than a monolayer thick and which is therefore likely to involve several atomic layers of the substrate. In fact, we interpret the data as indicating the formation of a titanium oxide interfacial layer, which will be discussed in the context of TEM evidence below.

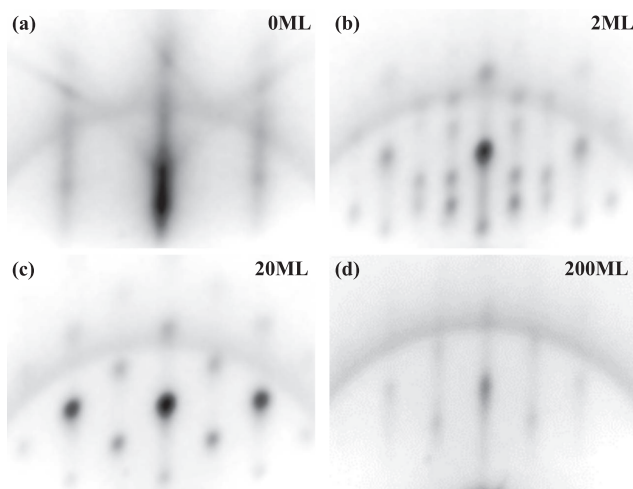


**FIG. 2.** RHEED diffraction patterns recorded throughout the growth of TiNiSn thin film on MgO(001) at 720 K. The images correspond to (a) the bare MgO substrate and approximate coverages of (b) 2 monolayers (ML), (c) 20 ML and (d) 200 ML. The electron beam was directed at a grazing angle to the (100) direction of the substrate.



The superstructure spots are apparent only at the 2 ML stage and disappear thereafter. Island growth persists throughout much of the subsequent deposition, but the diffuse background diminishes so that by a coverage of 20 ML [Fig. 2(c)], the surface crystal quality seems much improved. Figure 2(d) then shows the RHEED pattern after 200 ML deposition: this has partially recovered the streaky quality expected from a smooth, two-dimensional surface, which suggests a tendency toward gradual island coalescence, consistent with the broad, flat islands in Fig. 1(b). Throughout the entire deposition, the film retains a clearly crystalline and epitaxial character.

XRD measurements presented in Fig. 3 show the  $\theta - 2\theta$  diffraction pattern for a film deposited at 720 K. Only (00L) reflections are observed for the film, consistent with a single-crystal Heusler film with a (001) out-of-plane orientation that is coherent with the substrate. The remaining major reflection is accounted for by the MgO substrate, and minor contributions to the pattern close to the MgO(002) peak arise from the polycrystalline Pt capping layer deposited after thin film fabrication. Heusler reflections are found to be peaked between the expected positions for the bulk full and half-Heusler lattices, suggesting a non-stoichiometric mean composition. The position of the (004) reflection at  $62.03^\circ$  would suggest a mean

composition of  $\text{TiNi}_{1.3}\text{Sn}$ , showing a similar level of excess Ni to that discerned by EELS, but with an uncertainty relating to the approximation of applying a Vegard's law comparison to relaxed bulk values, in addition to the clear spatial inhomogeneities described below. Asymmetrical broadening of this peak, sloping in the direction of the bulk full-Heusler reflection, is attributed to the incoherent summation of diffraction from regions with different lattice constants due to variations in Ni concentration. Unlike the data discussed in the MBE study, which described observed XRD reflections using a pair of Gaussian profiles,<sup>26</sup> at least three pseudo-Voigt functions are required for a reasonable fit to the asymmetric peak, which is shown in Fig. 3(b). Although not a unique fit, it suggests the presence of at least three Heusler phases and may be more indicative of a narrow range of Ni-rich half-Heusler compositions. Accordingly, further improvements to the fit could be made by adding further components and the choice of three peaks here is justified on the basis of subsequent EELS measurements. The approximate compositions inferred from the fit are  $\text{TiNi}_{1.15}\text{Sn}$ ,  $\text{TiNi}_{1.5}\text{Sn}$ , and  $\text{TiNi}_2\text{Sn}$ , with relative breadths attributed to the quantity and geometric extent of each phase. Regions of the highest Ni content are expected to be the smallest and the sharper  $\text{TiNi}_{1.15}\text{Sn}$  peak corresponds to the majority phase. The Scherrer relation gives a mean domain

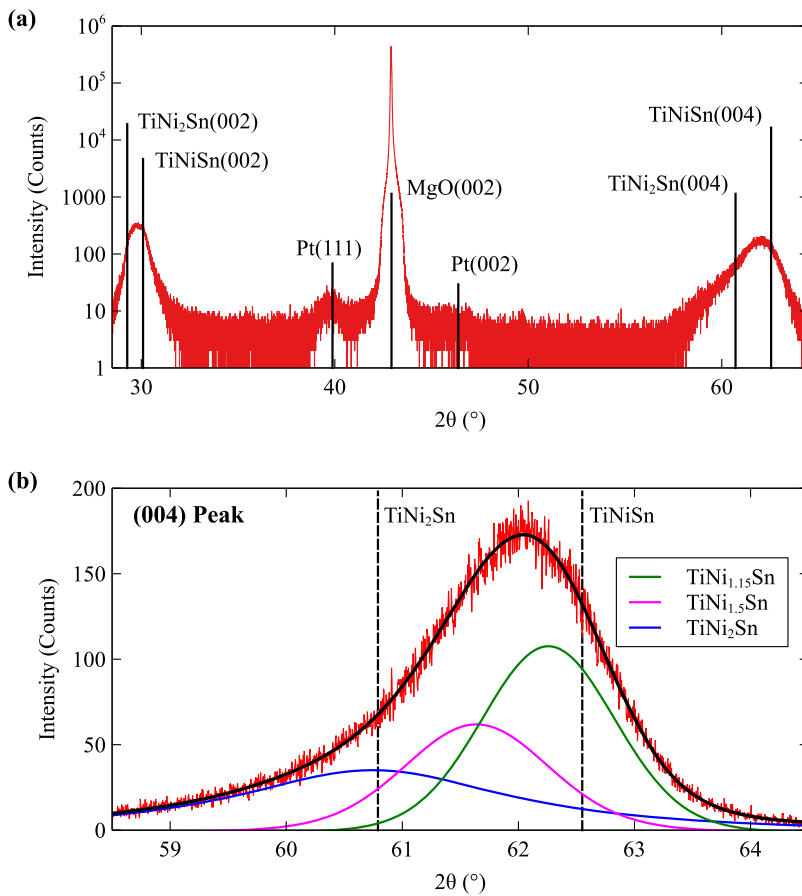


**FIG. 3.** (a) XRD  $\theta - 2\theta$  scan of  $\sim 100$  nm  $\text{TiNiSn}/\text{MgO}$  deposited by PLD at 720 K. Reflection angles based on the bulk lattice constants for  $\text{TiNiSn}$ ,  $\text{TiNi}_2\text{Sn}$ , Pt, and MgO are labeled. (b) The  $\text{TiNiSn}(004)$  reflection with bulk full and half-Heusler angles marked by dashed lines. A fit to the data and its three pseudo-Voigt profile components are also shown.

size of 31 nm, 14 nm, and 4 nm, respectively for these phases, indicating that the largest grains are those closest to the target composition.

We now turn to the TEM characterisation of a cross section through a typical film, grown at 720 K to a thickness of  $\sim 80$  nm. A low magnification overview of the film is presented in Fig. 4(a) and shows a fully dense, continuous film that lacks the obvious granularity of, for example, azimuthally disordered columnar growth. The trapezoidal features at the top of the film are identified as the broad, flat islands observed by AFM. Subtle variations in intensity running vertically throughout the film are attributed to either compositional variations or slight differences in diffractive scattering, both of which could arise from the intergrowth of islands that grew independently from distinct nucleation sites in the first few monolayers. Triangular features circled in Fig. 4(a) are likely nickel-stannide phases that form upon decomposition of the half-Heusler structure and are discussed further below. Convergent beam electron diffraction (CBED) patterns collected from three distinct regions are presented in Figs. 4(b)–4(d), using a focused beam of 1 nm diameter to acquire local diffraction information. The diffraction pattern from the substrate [Fig. 4(b)] shows the expected square symmetry with in-plane reciprocal lattice vectors that are coincident with those of the TiNiSn film [Fig. 4(d)], indicating epitaxy. The out-of plane diffraction spots collected from the film around 10 nm from the interface can be indexed to the expected, unstrained F-43m structure. The pattern collected at the interface, shown in Fig. 4(c), is dominated by a superposition of the patterns arising from the substrate and bulk film but with weak distinct spots, indicated by arrows, that are consistent with a slight out-of-plane expansion of the MgO (real space) lattice, together with a more subtle contraction of the in-plane lattice spacings. The diffraction peak spacings indicate an in-plane lattice contraction to  $4.17 \text{ \AA}$  accompanied by an out-of plane expansion to  $4.26 \text{ \AA}$ , thereby preserving the unit cell volume of MgO. The reduction in the substrate's

in-plane lattice constant at the interface is somewhat surprising as strain is generally expected to be accommodated in the growing thin film; the contraction is also more substantial than required to accommodate the nominal lattice mismatch and in fact switches from a situation where TiNiSn is deposited onto the 0.32% larger lattice of MgO to one where it is bonded to a substrate lattice that is 0.64% smaller. Both observations are attributed to chemical variations revealed by EELS, as discussed below. As the lattice spacings and strain are likely to evolve to their equilibrium values during the initial stages of deposition, this may explain the proclivity for three-dimensional island growth observed here and elsewhere.<sup>24,25</sup> A final important observation of Fig. 4(c) is that it shows no evidence of the surface reconstruction observed using RHEED during growth [Fig. 2(b)], which would again appear as additional spots at a third of the spacing of the in-plane lattice spots. The absence of a superstructure indicates that the modulation observed in RHEED reflected a transient surface reconstruction that was overcome upon subsequent deposition so that the overlayer retained a cubic structure. Lattice coherence is more evident in STEM imaging, and Fig. 5 shows a STEM High-Angle Annular Dark Field (STEM-HAADF) cross-sectional image of the MgO/TiNiSn interface that resolves atomic columns directly. Image contrast is dominated by differences in the atomic number, and the bright spots in the top half are Sn atoms, whilst the dim spots in the substrate are Mg. Figure 5(c) is a Fourier-filtered version of the same data that highlights the in-plane lattice spacings across the interface. Both images indicate a continuity of lattice lines with only four dislocations in the field of view.

STEM-EELS spectrum imaging was conducted in a similar region to that of Fig. 5(a) in order to provide spatially resolved chemical maps of the MgO/TiNiSn interface. The results are presented in Fig. 5(d) and indicate the relative proportions of the main elements, revealing the effects of substantial chemical reactions, including the presence of an interfacial nanolayer. Moving from the bottom to top through the

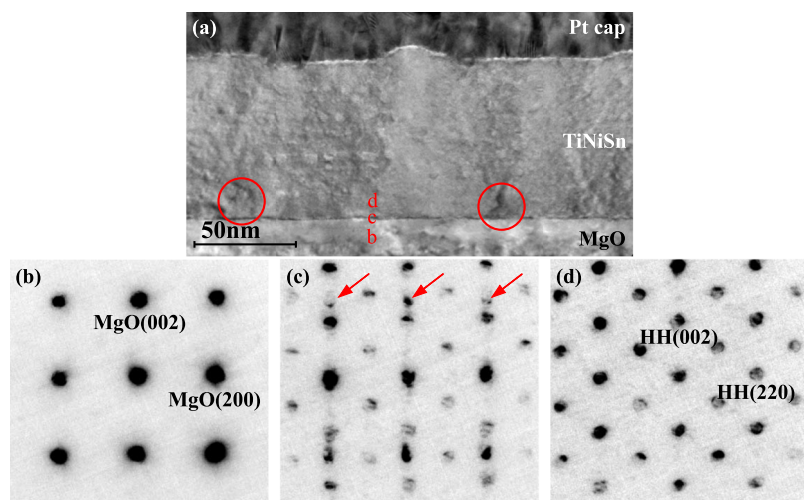


**FIG. 4.** (a) TEM image of a cross section of a TiNiSn film deposited on MgO(001) at 720 K with features identified as nickel stannides encircled in red. [(b)–(d)] Nanoprobe convergent beam electron diffraction (CBED) patterns collected along a MgO (010) direction and from positions marked approximately in the TEM image. Diffraction patterns correspond to (b) the MgO substrate, (d) the TiNiSn film, and (c) the interface between the film and the substrate. The scaling is the same for all images.

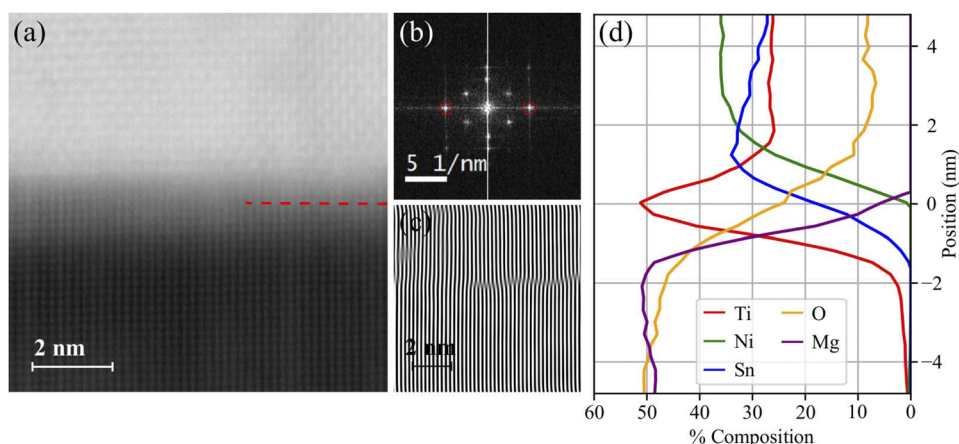


**FIG. 5.** (a) STEM-HAADF image of MgO/TiNiSn interface. The MgO substrate occupies the bottom half of the image. (b) Fourier transform and (c) Fourier-filtered image of (a) (using the spots circled in the fast Fourier transform) demonstrating crystalline and epitaxial ordering. (d) Result of elemental quantification across the interface aligned with the image in (a).

plot, the substrate has a clear 50:50 MgO composition but with a small quantity of Ti that extends up to 6 nm from the interface. The MgO signal drops to zero over a distance of 2 nm, forming a region that is substantially wider than would be expected for the extremely flat MgO substrates measured by AFM prior to deposition. It is therefore taken as evidence of substantial structural reorganisation and elemental diffusion in the initial stages of deposition. There is then a concentration of Ti at the interface, and this appears to be partially oxidised, having presumably drawn oxygen from the substrate. The oxygen signal itself extends further than that of the MgO and well into the half-Heusler film, only diminishing to zero outside of this data set. Ti enrichment at the interface produces complementary enhancement of the Ni and Sn concentrations immediately above. As can be seen in Fig. 5(d), the Sn concentration only drops to be equal to that of Ti about 5 nm beyond the interface. The enhancement in Ni, which here results in a local mean composition of  $\text{TiNi}_{1.38}\text{Sn}$ , persists further, beyond the range of this line profile and up to 10 nm from the interface.

Formation of a Ti-rich interfacial layer implies that the nature of the substrate's epitaxial template differs from that expected for clean MgO and might, therefore, lead to a loss of epitaxy and cause disordered, polycrystalline growth. However, the layer adopts a very similar lattice spacing to that of MgO and the Fourier filtered HAADF image in Fig. 5(c) does not indicate a disruption to the epitaxial relationship. It is also clear that the MgO subsurface region is chemically modified by Ti implantation up to 6 nm beneath the centre of the nanolayer. This is observed in both the EELS data and the STEM-HAADF image, which shows a clear band of intermediate intensity at the interface rather than an abrupt step between the relatively heavy TiNiSn and the relatively light MgO. It is possible that implantation arises from the impact of energetic species during PLD, but this would be expected to also apply to both Ni and Sn, which is not observed. We therefore attribute the Ti implantation to diffusion, in agreement with previous observations<sup>40</sup> that showed facile diffusion of Ti into MgO with cation substitution even at room

temperature. In Fig. 6, variations in the Ti  $L_{2,3}$  EELS edge across the nanolayer indicate a continuous change in the near-edge structure and as a consequence a change in the titanium oxidation state, moving from half-Heusler to interface to substrate. The chemical shift and fine structure of the Ti  $L_{2,3}$  edges in the half-Heusler are very similar to those of elemental Ti, in agreement with the covalent, uncharged nature of Ti within the half-Heusler alloy. Moving to the

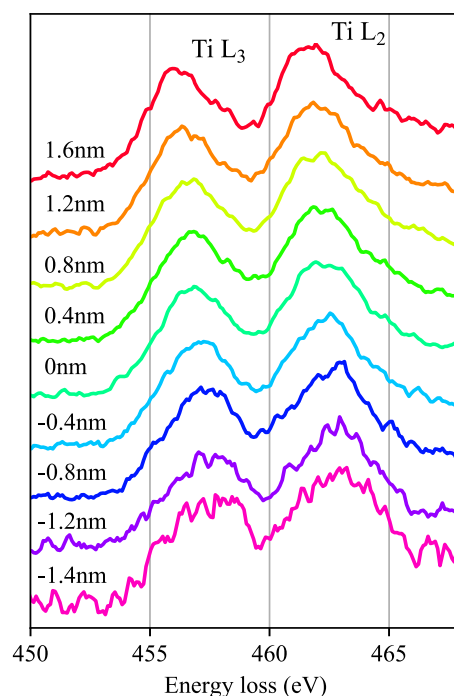


**FIG. 6.** Ti  $L_{2,3}$  near-edge spectra acquired from different positions scanning across the interface, with intensities normalised to the  $L_2$  maximum. The centre of the Ti-rich interface is marked as 0 nm so that positive positions denote points further into the Heusler film and negative toward the substrate.

interface layer, there is a small shift in the peak maxima to higher energy-losses as the proportion of oxide increases. In the interface and the substrate below, the position of the Ti  $L_3$  peak shifts to 457.4 eV, in excellent agreement with expectations for  $Ti^{2+}$  arising from a cubic  $TiO$  phase<sup>41</sup> (and inconsistent with the formation of  $TiO_2$ ). The near-edge structure observed for all positions below the half-Heusler are similar although with poorer signal-noise ratios due to the diminishing titanium content.

The formation of  $TiO$  which has a similar cubic structure to that of  $MgO$  and a very similar lattice constant ( $a_0 = 4.176 \text{ \AA}$ )<sup>42</sup> would explain the epitaxial relationship between  $TiNiSn$  and  $MgO$ . Although thin films of  $TiO$  on  $MgO$  have not been studied in detail previously, the surface termination of bulk titanium oxides is known to reconstruct to form a number of superstructure phases with the potential to lattice-match to the  $MgO$  substrate here.<sup>43,44</sup> Incorporation of Ti into the  $MgO$  substrate further increases the possibilities. A  $Mg$ - $Ti$ - $O$  spinel phase has been previously identified to have a coincidental lattice match with  $MgO$  (with a lattice parameter approximately twice that of  $MgO$ ),<sup>45</sup> and it is feasible that the transient reconstruction observed in RHEED is either a  $TiO$  reconstruction or a transient reconstructed  $Mg$ - $Ti$ - $O$  metastable phase. The substitution of Ti in the  $MgO$  lattice also explains the measured changes in lattice parameters at the interface if interpreted as an intermediate  $MgO$ : $TiO$  composition driving the in-plane lattice constant toward the smaller value for  $TiO$ .

Investigating the film on a broader scale, the STEM-HAADF image shown in Fig. 7(a) reveals that whilst the films are continuous and lack polycrystalline character, there is an unexpected network of nanoscale imperfections that appear as darker spots and hence comprise materials of lower atomic numbers than the main half-Heusler matrix. Elemental analysis was carried out in the sub-region indicated in Fig. 7(b) and reveals the matrix to have a broadly uniform composition but with distinct Ni-rich [green Fig. 7(b)] stripes below the dark regions observed in STEM. Quantification yielded a mean composition for the majority phase (the dull-green regions away from the interface or coloured stripes) of  $TiNi_{1.12}Sn$ , i.e., a half-Heusler with excess Ni, similar to the level of Ni attributed to the target. The dark regions observed in

STEM-HAADF, on the other hand, are nano-inclusions of titanium oxide. In Fig. 7(c), absolute quantification of EEL spectra shows an equal increase in the quantity of titanium and oxygen in the inclusion (at around 10 nm in the plot) compared to the half-Heusler phase, suggesting  $TiO$ . Assuming an isotropic form, we approximate the inclusions to be clusters of roughly spherical volumes that likely decorate the surface during deposition and will extend out of the plane of the TEM image by a similar amount to their observed diameter in the image plane. In the case of the inclusion shown in the line profile, absolute quantification results indicate approximately 1270 Ti atoms and a  $TiO$  volume of  $23 \text{ nm}^3$  with a diameter of 3.5 nm. Performing a similar analysis across the entire spectrum image indicates that approximately 2.5% of the film by volume is occupied by  $TiO$ . This level of oxide is consistent with that observed in the bulk target material, which subsequent study (not shown) indicates to exist as predominantly  $TiO_2$  and with a different particle size distribution to that observed in the films here. We surmise that it is likely that the target is the source of oxygen during growth and that the oxides are not transferred as complete nanoparticles during deposition. The presence of  $TiO$  rather than  $TiO_2$  is interesting because it has a structure that is coherent with the surrounding crystal matrix and allows epitaxy to continue, just as described above for the interfacial  $TiO$  layer. Perhaps this relatively unusual oxide phase is stabilised by lattice strain. A HAADF image resolving the atomic positions, dominated by Sn, which is heaviest, is presented in Fig. 8(a) with a Fourier-filtered image in Fig. 8(c). The latter clearly demonstrates continuity of the half-Heusler lattice around the oxide inclusion, with a small number of dislocations to accommodate strain. As the nanoinclusions are small enough to be embedded within the TEM lamella, their unique EEL spectra were isolated from that of the matrix using non-negative matrix factorisation (NMF). The two extracted spectra are presented in Fig. 8 and show a clear shift between the Ti within the inclusion and that of the matrix, with the inclusion again being assigned as  $TiO$  with  $Ti^{2+}$ .

Segregation of Ti into oxide inclusions perturbs the surrounding alloy composition, and the false-coloured spectrum image of Fig. 7 shows complementary green (Ni-rich) stripes immediately beneath each red ( $TiO$ ) region. If the flux of atomic species arriving at the substrate is stoichiometric and

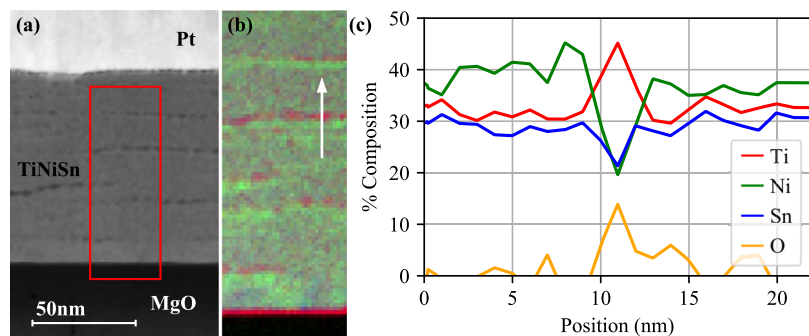


**FIG. 7.** (a) A STEM-HAADF cross-sectional image of a  $\sim 100 \text{ nm}$ -thick film grown at 720 K. A protective Pt capping layer was deposited immediately after deposition. (b) RGB colour-map determined from a spectrum image collected within the area marked by the red rectangle in (a), showing the distribution of Ti (red), Ni (green), and Sn (blue). (c) Plot of a single line profile through the quantification results marked by the white arrow in (b).



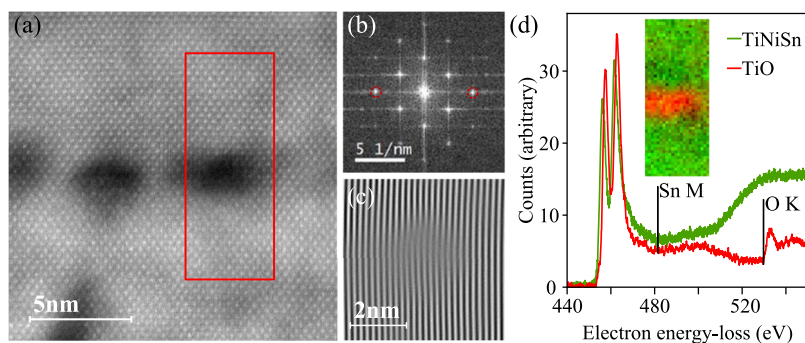


**FIG. 8.** (a) Atomic-column resolved HAADF image of TiO nanoinclusions in the TiNiSn film. STEM-EELS spectrum imaging was conducted within the red outline. (b) Fourier transform of (a) and (c) a Fourier-filtered image of the nanoinclusion showing the in-plane lattice spacing, demonstrating the continued epitaxy across the inclusion. (d) Results of the NMF procedure, showing the two most significant NMF factors contributing to the data in the region of Ti, Sn, and O EELS edges. The coloured inlay shows a false colour distribution of these two components across the spectrum image, clearly identifying the inclusion as TiO.

uniform throughout deposition, then it is likely that the segregation into Ni-rich and TiO phases occurs immediately after layers are deposited, producing the observed asymmetric elemental distribution. We speculate that trace oxygen arriving at the growing film is adsorbed and draws the Ti out of the underlying half-Heusler to decorate the growing surface with TiO nanoparticles that are subsequently buried. Sn does not appear to be as depleted in the region of the oxides [see Fig. 7(c)] and so is less accentuated in the residual underlying material. Determining an accurate composition for the Ni-enriched region is difficult because the region will, as with the oxides, be embedded and surrounded within the TEM lamella by matrix material; yet NMF decomposition is found to be unreliable because these two components differ only subtly in their Ni content. However, if the majority matrix phase is  $\text{TiNi}_{1.12}\text{Sn}$  and the Ni-enriched region is restricted to that immediately below the oxide inclusions, then the same geometric approximation applied to the TiO inclusions yields an average composition for the Ni-rich nanoinclusions of  $\sim\text{TiNi}_{1.8}\text{Sn}$ , which could account for the minority  $\text{TiNi}_{1.85}\text{Sn}$  fraction seen in XRD.

In some regions, greater extraction of Ti from the surrounding matrix cannot be supported without a collapse of the half-Heusler crystal structure, leading to decomposition to form a nickel stannide binary alloy phase, which occurs most notably at the substrate interface. One such region, taken from the same film as above, is illustrated in Fig. 9. In this region, the spectrum image yields a majority phase (i.e., excluding defects) of  $\text{TiNi}_{1.15}\text{Sn}$ , similar to that of Fig. 7(a), with the differences perhaps accounting for the vertical stripes in contrast seen in Fig. 4(a). Such variations in the majority phase Ni content across the film are reminiscent of the grain-by-grain variations seen in an earlier study of Cu-doped  $\text{TiNiSn}$ .<sup>23</sup> If the elemental flux during deposition is uniform, then such variations indicate the post-deposition lateral diffusion of Ni, which is intriguing. Turning to the defects, the spectrum image in Fig. 9(a) highlights Sn-rich (blue) regions immediately above the interfacial TiO (red) that relate to similar features encircled in Fig. 4(a). A line profile through the region—shown in Fig. 9(b)—clearly indicates a composition rich in Ni and Sn. (Note that the 0% deviation in Fig. 9(b) corresponds to the local majority phase of  $\text{TiNi}_{1.15}\text{Sn}$ .) The structure

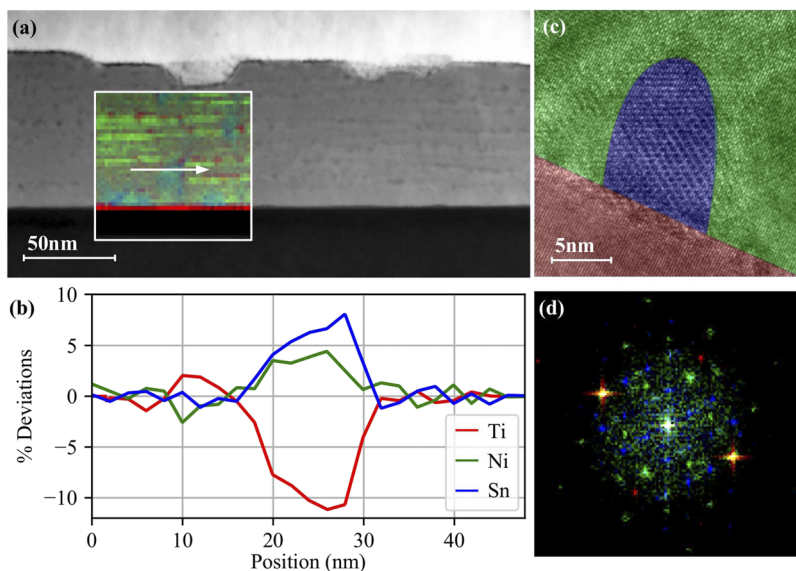


**FIG. 9.** (a) HAADF overview image of TiNiSn containing nickel-stannide phases. The false colour inlay is an RGB map showing the Ti, Ni, and Sn distributions, using the same colours as in (b). (b) Deviations from the matrix composition across the line segment marked by the white arrow in (a), which crosses a nanoscale grain of  $\text{Ni}_3\text{Sn}_4$ . (c) HRTEM image of a similar  $\text{Ni}_3\text{Sn}_4$  grain at the substrate interface (note that the TEM camera orientation makes the sample appear rotated with respect to the HAADF image). (d) Simulated diffraction pattern composed of Fourier transforms of regions in (c) with colours corresponding to the matching associated areas in (c). The FFT of the nickel stannide phase (blue) indicates a much larger lattice parameter than the half-Heusler phase and is consistent with  $\text{Ni}_3\text{Sn}_4$ .

of this Ni-Sn alloy can be discerned through analysis of the lattice-resolved high-resolution TEM image shown in Fig. 9(c), where the defect region, false-coloured in blue, has a different lattice to either the surrounding matrix or the substrate. The Fourier transform shown in Fig. 9(d) was used to distinguish distinct crystal regions—this has the appearance of a diffraction pattern and includes Fourier components from the substrate (coloured red), the matrix (coloured green), and the inclusion (coloured blue). Note the geometric alignment of all the spots, indicating an epitaxial relationship between all three components. The Ni-Sn alloy's Fourier components can be indexed using the structure of  $\text{Ni}_3\text{Sn}_4$  observed on the  $[110]$  zone axis. This nickel stannide phase is one of two possible phases predicted in recent *ab initio* thermodynamical calculations;<sup>46</sup> no evidence has been found for the other predicted phase,  $\text{Ni}_3\text{Sn}_2$ . The inhomogeneity represented by this relatively large,  $\sim 10$  nm-high inclusion is difficult to reconcile with the uniform flux expected during PLD, and it is unclear if its formation is driven by an irregularity in the substrate, a fluctuation in the arriving flux during deposition to produce a NiSn “seed” island or the result of inhomogeneous diffusion post-deposition. However, the coincidence of an apparent dip in the surface profile above the inclusion—a gap between the flat islands observed by AFM—does suggest that the half-Heusler material on either side of the inclusion nucleated separately and merged together as the film grew.

We have demonstrated that pulsed laser deposition of off-stoichiometric TiNiSn on MgO(001) between substrate temperatures of 620 K and 720 K results in smooth, epitaxial films, albeit with some limited three-dimensional character that diminishes with increasing film thickness. Our results suggest that an initial three dimensional growth mode arises as a consequence of surface reactions that substantially roughen the substrate immediately upon deposition and thereby limit adatom mobility. These reactions most notably involve the extraction of oxygen from the substrate and titanium from the film to form a titanium monoxide phase and a Ti-implanted MgO surface region, both of which retain an epitaxial relationship with the bulk substrate and which therefore do not impede subsequent epitaxy of the deposited half-Heusler film. The introduction of a buffer layer, such as epitaxial vanadium, could act as a barrier to prevent this interaction with the substrate and will be the subject of future work. Growth beyond the interfacial layer leads to the formation of a narrow range of half-Heusler compositions that manifest in broadened XRD peaks. From EELS quantification, however, the distributions of phases is weighted to form spatially distinct regions with mean compositions of  $\text{TiNi}_{1.12}\text{Sn}$  for the matrix,  $\text{TiNi}_{1.38}\text{Sn}$  for a thin Ni-enriched layer above the interface, and  $\text{TiNi}_{1.8}\text{Sn}$  for the Ni-rich nanoinclusions, occupying volume fractions of 78.4%, 8.1%, and 11%, respectively. In addition, the TiO oxide phase, not including the interfacial oxide that likely draws oxygen from the substrate itself, occupies a 2.5% volume fraction that we attribute to oxides present in the PLD target. These Heusler compositions differ slightly from the predictions made from the XRD data, where the predicted

compositions are  $\text{TiNi}_{1.15}\text{Sn}$ ,  $\text{TiNi}_{1.5}\text{Sn}$ , and  $\text{TiNi}_2\text{Sn}$ . However, as has been discussed elsewhere,<sup>47</sup> the TiNiSn half-Heusler lattice does not expand linearly with excess nickel concentration and interpreting the XRD data with Vegard's law is therefore only indicative.

Trace oxygen present during PLD growth, most likely from titanium oxides in the target material, results in the formation of cubic titanium monoxide nanoinclusions which, curiously, do not disrupt epitaxy but do appear to drive the formation of Ni-rich half-Heusler phases and Sn-rich binary phases. It can be assumed that these inclusions will be less problematic if more pure PLD targets can be produced. It is interesting to note that the presence of neither TiO nor  $\text{Ni}_3\text{Sn}_4$  was observed by XRD and both could therefore be easily overlooked without the spatial resolution of TEM techniques. Functionally, the presence of titanium oxides is not anticipated to impair performance, as indicated by experimental measurements<sup>17</sup> and theoretical calculations.<sup>46</sup>

Spontaneous phase segregation of the Ni-rich half-Heusler target material was to be expected from the literature, with a tendency to form crystals with compositions close to the nominal half-Heusler or full-Heusler. However, the nature of the segregation observed here is interesting. Although modest segregation into vertical stripe domains has been observed, the variation in the Ni content (as described by the “majority” phases discussed above) is slight. On the other hand, a clear motif of the films is the proximity of titanium oxides with regions of more pronounced Ni enrichment.  $\text{TiNi}_{1.38}\text{Sn}$  was observed immediately above the interfacial oxide layer, and  $\text{TiNi}_{1.8}\text{Sn}$  tended to form beneath TiO inclusions. The latter is consistent with the smaller enthalpy of formation of the full-Heusler phase,<sup>48</sup> resulting in greater stability compared to the half-Heusler. Stabilisation of the  $\text{TiNi}_{1.38}\text{Sn}$  phase through a chemical interaction with the substrate and, perhaps, the epitaxial relationship with the Ti-doped MgO interfacial layer, however, highlights the difference between the thermodynamically equilibrated state and materials deposited under kinetically limited conditions and deserves further investigation.

The nanostructuring and oxide formation observed here are of key importance in the understanding of phase segregation effects in thermoelectric half-Heusler alloys, where the micro-/nanostructure of the material can have a key role in limiting the thermal conductivity and improving thermoelectric performance. Here, we observe phase segregation that appears to be driven by a proximity to TiO phases and the subsequent diffusion of Ti out of the majority matrix. We envisage both these results and the methods used for their characterisation, being of relevance to a broad range of other Heusler alloy systems.

This work was funded by the Engineering and Physical Sciences Research Council of the UK through Grant Nos. EP/N017218/1 and EP/N509668/1. Thanks are given to Dr. Matthew Steer for his assistance with XRD measurements. Raw data relating to the study can be found at <http://dx.doi.org/10.5525/gla.researchdata.711>.

## REFERENCES

- <sup>1</sup>R. A. de Groot, F. M. Mueller, P. G. van Engen, and K. H. J. Buschow, *Phys. Rev. Lett.* **50**, 2024 (1983).
- <sup>2</sup>I. Galanakis, P. H. Dederichs, and N. Papanikolaou, *Phys. Rev. B* **66**, 174429 (2002).
- <sup>3</sup>*Heusler Alloys*, Springer Series in Materials Science, edited by C. Felser and A. Hirohata (Springer International Publishing, Cham, Switzerland, 2016), Vol. 222.
- <sup>4</sup>M. Dresselhaus, G. Chen, M. Tang, R. Yang, H. Lee, D. Wang, Z. Ren, J.-P. Fleurial, and P. Gogna, *Adv. Mater.* **19**, 1043 (2007).
- <sup>5</sup>G. J. Snyder and E. S. Toberer, *Nat. Mater.* **7**, 105 (2008).
- <sup>6</sup>A. J. Minnich, M. S. Dresselhaus, Z. F. Ren, G. Chen, F. Steglich, G. Zeng, J. H. Bahk, J. E. Bowers, J. M. O. Zide, A. C. Gossard, G. Chen, Z. Ren, G. Chen, Z. Ren, and Z. Ren, *Energy Environ. Sci.* **2**, 466 (2009).
- <sup>7</sup>Lawrence-Livermore National Laboratory, "Estimated U.S. energy consumption in 2015," <https://flowcharts.llnl.gov/>, 2016; accessed 31 March 2017.
- <sup>8</sup>J.-W. G. Bos and R. A. Downie, *J. Phys.: Condens. Matter* **26**, 433201 (2014).
- <sup>9</sup>R. A. Downie, D. A. MacLaren, R. I. Smith, and J. W. G. Bos, *Chem. Commun.* **49**, 4184 (2013).
- <sup>10</sup>W. G. Zeier, J. Schmitt, G. Hautier, U. Aydemir, Z. M. Gibbs, C. Felser, and G. J. Snyder, *Nat. Rev. Mater.* **1**, 16032 (2016).
- <sup>11</sup>K. Bartholomé, B. Balke, D. Zuckermann, M. Köhne, M. Müller, K. Tarantik, and J. König, *J. Electron. Mater.* **43**, 1775 (2014).
- <sup>12</sup>R. Akram, Q. Zhang, D. Yang, Y. Zheng, Y. Yan, X. Su, and X. Tang, *J. Electron. Mater.* **44**, 3563 (2015).
- <sup>13</sup>H. Hazama, M. Matsubara, and R. Asahi, *J. Electron. Mater.* **41**, 1730 (2012).
- <sup>14</sup>T. Katayama, S. W. Kim, Y. Kimura, and Y. Mishima, *J. Electron. Mater.* **32**, 1160 (2003).
- <sup>15</sup>H. Muta, T. Kanemitsu, K. Kurosaki, and S. Yamanaka, *J. Alloys Compd.* **469**, 50 (2009).
- <sup>16</sup>M. Onoue, F. Ishii, and T. Oguchi, *J. Phys. Soc. Jpn.* **77**, 054706 (2008).
- <sup>17</sup>R. A. Downie, R. I. Smith, D. A. MacLaren, and J.-W. G. Bos, *Chem. Mater.* **27**, 2449 (2015).
- <sup>18</sup>J. E. Douglas, C. S. Birkel, M.-S. Miao, C. J. Torbet, G. D. Stucky, T. M. Pollock, and R. Seshadri, *Appl. Phys. Lett.* **101**, 183902 (2012).
- <sup>19</sup>K. Kirievsky, Y. Gelbstein, and D. Fuks, *J. Solid State Chem.* **203**, 247 (2013).
- <sup>20</sup>J. Callaway, *Phys. Rev.* **113**, 1046 (1959).
- <sup>21</sup>P. G. Klemens, *Proc. Phys. Soc. Sect. A* **68**, 1113 (1955).
- <sup>22</sup>H. Goldsmid and A. Penn, *Phys. Lett. A* **27**, 523 (1968).
- <sup>23</sup>S. A. Barczak, J. E. Halpin, J. Buckman, R. Decourt, M. Pollet, R. I. Smith, D. A. MacLaren, and J.-W. G. Bos, *ACS Appl. Mater. Interfaces* **10**, 4786 (2018).
- <sup>24</sup>T. Jaeger, C. Mix, M. Schwall, X. Kozina, J. Barth, B. Balke, M. Finsterbusch, Y. U. Idzerda, C. Felser, and G. Jakob, *Thin Solid Films* **520**, 1010 (2011).
- <sup>25</sup>J. K. Kawasaki, T. Neulinger, R. Timm, M. Hjort, A. A. Zakharov, A. Mikkelsen, B. D. Schultz, and C. J. Palmstrøm, *J. Vac. Sci. Technol., B: Nanotechnol. Microelectron.: Mater., Process., Meas., Phenom.* **31**, 04D106 (2013).
- <sup>26</sup>A. Rice, J. Kawasaki, N. Verma, D. Pennachio, B. Schultz, and C. Palmstrøm, *J. Cryst. Growth* **467**, 71 (2017).
- <sup>27</sup>D. B. Chrisey and G. K. Hubler, *Pulsed Laser Deposition of Thin Films* (John Wiley & Sons, New York, 1994).
- <sup>28</sup>M. Matsubara, H. Azuma, and R. Asahi, *J. Electron. Mater.* **40**, 1176 (2011).
- <sup>29</sup>C. Duriez, C. Chapon, C. Henry, and J. Rickard, *Surf. Sci.* **230**, 123 (1990).
- <sup>30</sup>C. Arnold and M. Aziz, *Appl. Phys. A: Mater. Sci. Process.* **69**, S23 (1999).
- <sup>31</sup>M. Schaffer, B. Schaffer, and Q. Ramasse, *Ultramicroscopy* **114**, 62 (2012).
- <sup>32</sup>J. Scott, P. Thomas, M. MacKenzie, S. McFadzean, J. Wilbrink, A. Craven, and W. Nicholson, *Ultramicroscopy* **108**, 1586 (2008).
- <sup>33</sup>C. Jeanguillaume and C. Colliex, *Ultramicroscopy* **28**, 252 (1989).
- <sup>34</sup>J. Bobynko, I. MacLaren, and A. J. Craven, *Ultramicroscopy* **149**, 9 (2015).
- <sup>35</sup>A. J. Craven, J. Bobynko, B. Sala, and I. MacLaren, *Ultramicroscopy* **170**, 113 (2016).
- <sup>36</sup>A. J. Craven, B. Sala, J. Bobynko, and I. MacLaren, *Ultramicroscopy* **186**, 66 (2018).
- <sup>37</sup>R. Egerton, *Electron Energy-Loss Spectroscopy in the Electron Microscope* (Springer, Boston, MA, USA, 2011).
- <sup>38</sup>F. de la Peña, T. Ostasevicius, V. T. Fauske, P. Burdet, P. Jokubauskas, M. Nord, E. Prestat, M. Sarahan, K. E. MacArthur, D. N. Johnstone, J. Taillon, J. Caron, T. Furnival, A. Eljarrat, S. Mazzucco, V. Migunov, T. Aarholt, M. Walls, F. Winkler, B. Martineau, G. Donval, E. R. Hoglund, I. Alxneit, I. Hjorth, L. F. Zagonel, A. Garmannslund, C. Gohlke, I. Iyengar, and H.-W. Chang (2017). "Hyperspy 1.3," Zenodo. <https://doi.org/10.5281/zenodo.583693>
- <sup>39</sup>P. Politi, G. Grenet, A. Marty, A. Ponchet, and J. Villain, *Phys. Rep.* **324**, 271 (2000).
- <sup>40</sup>T. Suzuki and R. Souda, *J. Phys. Chem. B* **103**, 5747 (1999).
- <sup>41</sup>E. Stoyanov, F. Langenhorst, and G. Steinle-Neumann, *Am. Mineral.* **92**, 577 (2007).
- <sup>42</sup>C. Zhang, F. Hao, G. Gao, X. Liu, C. Ma, Y. Lin, Y. Yin, and X. Li, *npj Quantum Mater.* **2**, 2 (2017).
- <sup>43</sup>A. I. Gusev, *J. Exp. Theor. Phys.* **120**, 851 (2015).
- <sup>44</sup>A. A. Valeeva, A. A. Rempel, and A. I. Gusev, *Inorg. Mater.* **37**, 603 (2001).
- <sup>45</sup>T. Kubo and H. Nozoye, *Thin Solid Films* **394**, 150 (2001).
- <sup>46</sup>A. Berche and P. Jund, *Intermetallics* **92**, 62 (2018).
- <sup>47</sup>V. Romaka, P. Rogl, L. Romaka, Y. Stadnyk, N. Melnychenko, A. Grytsiv, M. Falmbigl, and N. Skryabina, *J. Solid State Chem.* **197**, 103 (2013).
- <sup>48</sup>J. E. Douglas, C. S. Birkel, N. Verma, V. M. Miller, M.-S. Miao, G. D. Stucky, T. M. Pollock, and R. Seshadri, *J. Appl. Phys.* **115**, 043720 (2014).